Solid State Sciences 107 (2020) 106352

Contents lists available at ScienceDirect

Solid State Sciences

journal homepage: http://www.elsevier.com/locate/ssscie

Structural, physical and photocatalytic properties of mixed-valence double-perovskite $Ba_2Pr(Bi,Sb)O_6$ semiconductor synthesized by citrate pyrolysis technique

Arisa Sato [a], Michaki Matsukawa [a,*], Haruka Taniguchi [a], Shunsuke Tsuji [a], Kazume Nishidate [a], Sumio Aisawa [a], Akiyuki Matsushita [b], Kun Zhang [b]

[a] Faculty of Science and Engineering, Iwate University, Morioka, 020-8551, Japan
[b] National Institute for Materials Science, Ibaraki, 305-0047, Japan

A B S T R A C T

We demonstrated crystal structures, magnetic, optical, and photocatalytic properties of the B-site substituted double perovskite $Ba_2Pr(Bi_{1-x}Sb_x)O_6$ ($x = 0$, 0.1, 0.2, 0.5 and 1.0) synthesized by the citrate pyrolysis method. The single-phase polycrystalline samples with the light Sb substitution crystallized in a monoclinic structure ($I2/m$). Magnetization measurements on all the samples showed that the effective magnetic moments are concentrated around 3 μ_B, indicating the valence mixing states between Pr^{3+} and Pr^{4+}. The magnitudes of band gap energy for the two end member samples were estimated from the optical measurements to be $E_g = 1.06$ eV at $x = 0$ and 2.71 eV at $x = 1.0$. The $Ba_2Pr(Bi_{1-x}Sb_x)O_6$ ($x = 0$, and 0.1) powders obtained by the present technique exhibited enhanced photocatalytic activities when compared to the same compounds prepared by the conventional solid state method. Our findings suggest that the higher photocatalytic activities strongly depend on powder preparation methods as well as the band gaps and photogenerated charge separation.

1. Introduction

A large number of double perovskite oxides $A_2B'B''O_6$ have been widely studied due to their attractive physical properties and potential applications [1]. For example, the A_2FeMoO_6 compound shows negative tunneling magnetoresistance effect at room temperature, which is of great interest with a wide range of applications in magnetic devices [2]. Furthermore, multiferroic double perovskite oxides with a coupling between spontaneous ferroelectric polarization and ferromagnetic ordering are promising materials from view points of physics and its applications [3]. Some of semiconducting $A_2B'B''O_6$ compounds exhibit photocatalytic properties such as hydrogen generation by water splitting and are taken as alternative materials for TiO_2 oxide [4,5]. In particular, Ba_2PrBiO_6 has been shown to possess high photocatalytic activity, which is probably related to the valence mixing [6,7]. A previous study on the magnetic states of the Ba_2PrBiO_6 compound suggests an anomalous valence situation for Pr ions [8]. The complicated ground states of rare earth ions such as the Pr ion under the crystal field effect remain open question, not only in the physical properties of the double perovskite compound, but also from the view point of physics of the 4*f* electron systems.

There are significant factors such as charge and size differences between B′ and B″ sites, to determine the B-site ordering of the double perovskite oxide [1]. Increase in lattice strain and/or increase in the electrostatic repulsion overcome the entropy contribution toward disordering, causing the alternate arrangement. For $A_2^{2+}B^{'3+}B^{''5+}O_6$ composition, the B sites tend to order with increasing the ion size difference $\triangle r_B = r_{B'} - r_{B''}$. If $\triangle r_B > 0.2$ Å, it is well known that the B sites of the compounds are almost ordered alternately in the all crystallographic axes [1]. In the $Ba_2^{2+}Pr^{3+}Bi^{5+}O_6$ compound, the B-site ionic radius difference $\triangle r_B = 0.23$ Å meets the above condition, suggesting the B-site ordering. ($r_{B'}$ (Pr^{3+}) = 0.99 Å and $r_{B''}$ (Bi^{5+}) = 0.76 Å [9].) In this paper, we report x-ray diffraction measurements, magnetic susceptibilities, diffuse reflectance spectra, and 2-propanol (IPA) degradation for the $Ba_2Pr(Bi_{1-x},Sb_x)$ O_6 compounds, to determine the crystal structures, magnetic, optical, and photocatalytic properties of B-site substituted double perovskite oxides. A citrate pyrolysis technique is similar to nitrate combustion synthesis methods [10] and an unique route to prepare reactive precursor mixtures through an ignition process of concentrated aqueous solution including metallic ions of stoichiometric composition. For $YBa_2Cu_4O_8$ with T_c = 80 K and its related cuprate oxide compounds, it has been reported that high-quality single-phase polycrystalline materials are synthesized under ambient pressure of oxygen gas at lower annealed temperatures [11,12]. We

* Corresponding author.
E-mail address: matsukawa@iwate-u.ac.jp (M. Matsukawa).

https://doi.org/10.1016/j.solidstatesciences.2020.106352
Received 10 May 2020; Received in revised form 3 July 2020; Accepted 3 July 2020
Available online 14 July 2020

expect that this procedure enables to synthesize highly homogeneous and fine powders. As for one approach to developing efficient visible light driven photocatalysts, it is desirable to adjust the band gaps of their semiconductors to utilize a wide range of visible light [13,14]. According to this approach, they are controlled by the effect of Sb substitution on the parent material. In addition to it, another approach for high performance is to enhance the photogenerated charge separation in the photocatalystic materials, to avoid charge recombination between electron and hole [13,15]. In our research, the valence mixing states between Pr^{3+} and Pr^{4+} are closely related to the photo induced charge separation.

2. Experiment

Polycrystalline samples of Sb-substituted Ba_2PrBiO_6 were synthesized by using the citrate pyrolysis technique. In the first step, stoichiometric mixtures of high purity $BaCO_3$, Pr_6O_{11}, Bi_2O_3, and Sb were dissolved in a nitric acid solution at 70–80 °C. After adding citric acid and neutralizing it by aqueous ammonia, we then obtained the porous products through the self-ignition process using halogen lamp stirrer. In the next step, the precursors were ground and resultant fine powders were annealed in air at 900–1000 °C for 48–96 h, in order to synthesize the Ba_2PrBiO_6 double perovskite phase. For scanning electron microscope measurements, the Ba_2PrBiO_6 polycrystalline film on Ag substrate was fabricated from the single-phase powders by an electrophoretic deposition technique. The electrophoretic deposition was conducted in the acetone and iodine bath under the application of electric voltage up to 300 V for 120 s [16]. We set Pt and Ag plates as anode and cathode electrodes, respectively. We performed X-ray diffraction measurements on the produced samples at room temperature with an Ultima IV diffractometer (Rigaku) using Cu-Kα radiation. The lattice parameters were estimated from the x-ray diffraction data using the RIETAN-FP program. The Brunauer-Emmett-Teller (BET) surface area of the powder samples was evaluated using a surface area analyzer (BELSORP-mini II, Microtrac).

Optical spectra were measured by a diffuse reflectance method using a spectrophotometer (Hitachi U-3500) and $BaSO_4$ was used as the reference material. The optical band gaps for the powder samples were evaluated from reflectance spectral data using the conventional Kubelka-Munk functions [6,18]. The *dc* magnetization was measured at a magnetic field of 0.1 T under the field cooling process using a superconducting quantum interference device magnetometer (MPMS,

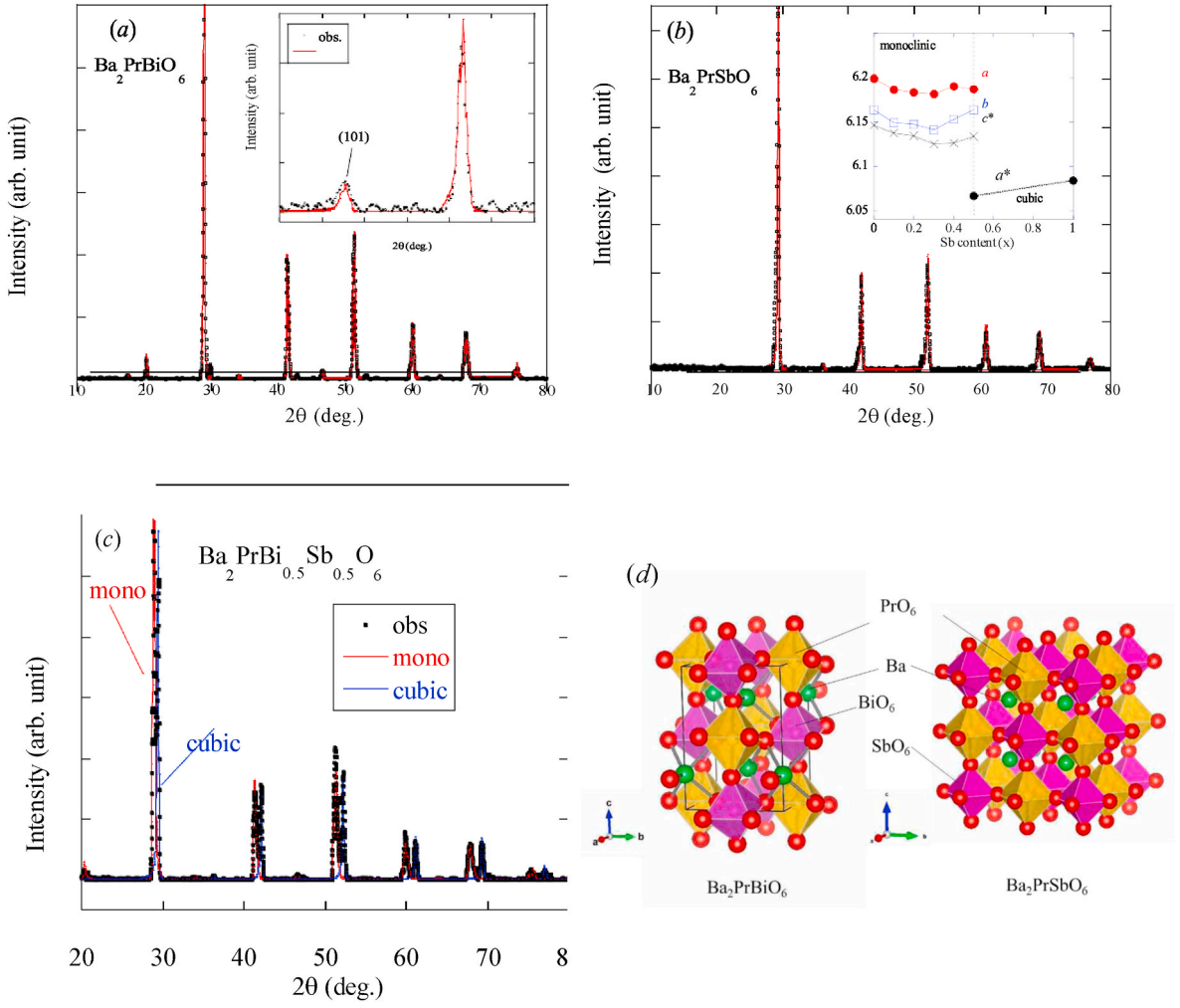

Fig. 1. (color online) X-ray diffraction patterns for the two end-member citrate samples, (*a*) Ba_2PrBiO_6 and (*b*) Ba_2PrSbO_6. In addition, the data for the intermediate sample $Ba_2Pr(Bi_{0.5},Sb_{0.5})O_6$ are given in (*c*). The calculated profiles based on the monoclinic and cubic structure models are shown in (*a*) and (*b*), respectively. The insets of (*a*) and (*b*) display the enlarged diffraction profiles and the lattice parameters as a function of Sb content. In the inset of (*b*), for monoclinic and cubic structures, $c^* = c/\sqrt{2}$ and $a^* = a/\sqrt{2}$, respectively. In (*c*). the red and blue plots are responsible for the monoclinic and cubic structure models, respectively. (*d*) Crystal structures for the two end-member samples, Ba_2PrBiO_6 and Ba_2PrSbO_6. The left and right pictures represent the ideal monoclinic and cubic structures, respectively. Bi(or Sb)O_6 and PrO_6 octahedra are connected by corner-sharing with each other. (For interpretation of the references to color in this figure legend, the reader is referred to the Web version of this article.)

Quantum Design). We conducted the gaseous 2-propanol (IPA) degradation experiment, to evaluate photocatalytic activities of the powder samples (in detail, refer to Refs. [6,19]). The powder (about 1 g) was placed on the bottom of a small glass cell and its cell was set in a 0.5-L glass reactor vessel. After removing impurities from the vessel through filling a dry air, the dilute IPA gas (5 cc) was injected into its vessel using a syringe. We started illuminating the visible light after the IPA concentration remained constant, which implied that the IPA gas finished absorbing on the surface of particles. The visible light was obtained using a 300W Xe lamp equipped with UV and IR filtering functions (Cermax LX300F, Excelitas Technologies). The illuminating spectra of the Xe lamp are limited in the visible wavelength range between 390 and 780 nm (see supplementary data Fig. S1). It is well known that the IPA gas under photocatalytic reaction is finally decomposed into CO_2 [19]. Accordingly, the CO_2 concentration was measured as a function of irradiation time using a gas chromatography system (GC-2014, Shimazu Co.)

3. Results and discussion

The X-ray diffraction patterns for the two end-member oxides, Ba_2PrBiO_6 and Ba_2PrSbO_6, are shown in Fig. 1 (*a*) and (*b*), respectively. For the parent Ba_2PrBiO_6 with a monoclinic structure (the space group $I2/m$), the lattice parameters are estimated to be $a = 6.2038$ Å, $b = 6.1689$ Å, $c = 8.7011$ Å and $\beta = 89.7303^{\circ}$ from the x-ray diffraction data using RIETAN-FP program, which are in good agreement with previous data [8,17]. The emergence of (101) reflection (the inset of Fig. 1 (*a*)) indicates B-cation ordering which is characteristic of the ordered double-perovskite structure. In particular, the tiny profiles around the (101) peak are well described by the least squared method based on RIETAN-FP when we set B site ordering to be ~70 %. This estimated ratio is nearly in good agreement with the published value (~75 %) [8]. The polycrystalline samples for $x < 0.5$ are formed in almost single phases of the monoclinic structure, while the $x = 1.0$ sample crystallizes in a cubic structure with the space group $Fm\bar{3}m$. Substitution of the smaller Sb^{5+} (0.60 Å) ion at the Bi^{5+} (0.76 Å) site causes a monotonic decrease in the lattice parameters as displayed in the inset of Fig. 1 (*b*). Upon further increasing Sb content, the x-ray diffraction patterns for $x = 0.5$ sample exhibit a two-phase mixture of monoclinic and cubic structures (Fig. 1(*c*)). The double main peaks responsible for the monoclinic and cubic phases are almost comparable and they are in the ratio of 56 % ($I2/m$) to 44 % ($Fm\bar{3}m$). For Ba_2PrSbO_6, we obtain the lattice parameters $a = 8.6042$ Å and $\alpha = 90^{\circ}$. Our result is qualitatively different from the rhombohedral structure as previously reported [20,21]. The differences in crystal structures are attributed to the tolerance factors which are associated with the mixed valence state of Pr ions. We will discuss this interesting issue following the magnetic data. The crystal structures for the two end-member samples, Ba_2PrBiO_6 and Ba_2PrSbO_6 are shown in Fig. 1(*d*), corresponding to the monoclinic and cubic structures, respectively. The Bi(or Sb)O_6 and PrO_6 octahedra are connected by corner-sharing with each other. However, the corresponding (101) peak observed at the low Sb substituted sample is strongly suppressed at $x = 1.0$, indicating the B-site disordering.

The microstructures of the parent samples prepared by the citrate pyrolysis and solid-state reaction methods are shown in Fig. 2. (For the Sb substituted samples with $x = 0.1$ and 1.0, see supplementary data Fig. S2) The particles of the former sample have an average size in the range of about 0.2–0.5 μm. On the other hand, the particle diameters of the latter sample are on a micron order scale and about one-order grater than those of the former. The citrate pyrolysis process provides homogeneously dispersed grains with sub micron size in comparison to the conventional solid-state procedure. We suspect that the substitution of Sb ion at Bi sites promotes the refinement of powder samples as shown in Fig. S2. This finding is probably related to the larger surface area for the Sb substituted samples.

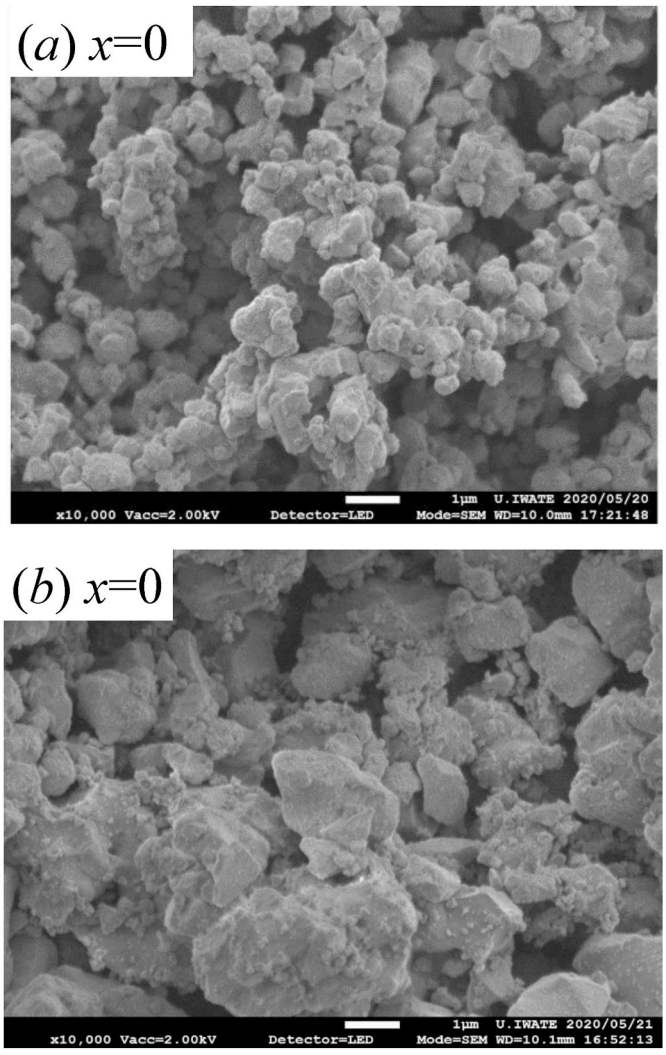

Fig. 2. (color online) SEM images of Ba_2PrBiO_6 powders. (*a*) citrate pyrolysis and (*b*) solid-state reaction techniques. (For $Ba_2Pr(Bi_{1-x},Sb_x)O_6$ with $x = 0.1$, and 1.0, see supplementary data Fig. S2).

The inverse magnetic susceptibility data (χ^{-1}) for the $Ba_2Pr(Bi_{1-x}, Sb_x)$ O_6 compounds ($x = 0$, 0.5 and 1.0) are shown in Fig. 3 as a function of temperature at a magnetic field of 0.1 T. All the measured samples exhibit no signature of magnetic ordering over a wide range of temperatures. From the magnetization data at high temperatures above 200 K, we estimate the effective magnetic moment according to the Curie-Weiss law, $\chi = C/(T - \Theta)$. Here, C and Θ are the Curie constant and Curie temperature. The value of effective magnetic moment μ_{eff} is evaluated by using the following formula,

$$C = N\mu_{\mathrm{eff}}^2\mu_B^2 \Big/ 3k_B$$

where N and μ_B denote the number of magnetic atom per mol and the Bohr magneton, respectively. Performing the calculation for the parent and lightly Sb substituted samples, we obtain that $\mu_{\mathrm{eff}} = 3.07\ \mu_B$ and 3.05 μ_B in $x = 0$ and $x = 0.1$ cases, respectively. As shown in the inset of Fig. 3, the magnetic moment is almost stable against the Sb substitution. Next, we try to estimate the ratio of the Pr^{3+} and Pr^{4+} ions using the equation

$$\mu_{\mathrm{eff}}^2 = y\mu_{\mathrm{eff}}^2(\mathrm{Pr}^{3+}) + (1-y)\mu_{\mathrm{eff}}^2(\mathrm{Pr}^{4+})$$

where $\mu_{\mathrm{eff}}(Pr^{3+}) = 3.58\ \mu_B$ and $\mu_{\mathrm{eff}}(Pr^{4+}) = 2.54\ \mu_B$. For the parent sample, we obtain that the ratio of Pr^{3+} and Pr^{4+} ions is 0.47 : 0.53. For $x = 0.1$, Pr^{3+}: $Pr^{4+} = 0.45 : 0.55$. For all the samples, the magnetic data

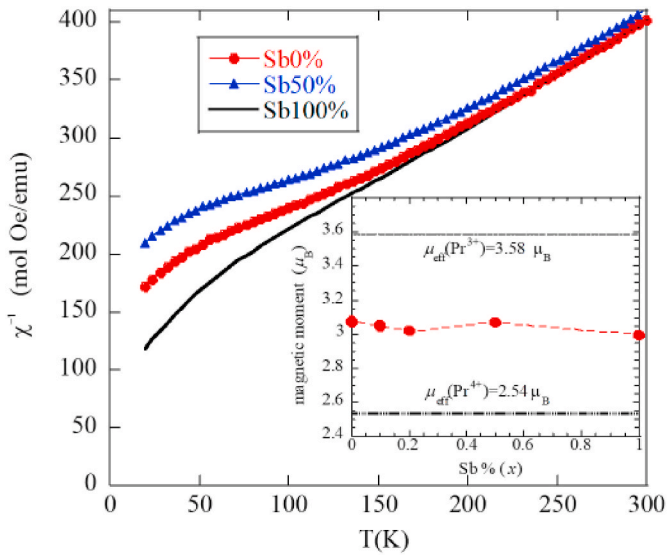

Fig. 3. (color online) Inverse magnetic susceptibility vs temperature. (χ^{-1}) for $Ba_2Pr(Bi_{1-x},Sb_x)$ O_6(x = 0, 0.5, and 1.0). The inset denotes the effective magnetic moment plotted as a function of Sb content. The value of μ_{eff} is evaluated using the Curie-Weiss law. The lower and upper limits represent $\mu_{eff}(Pr^{4+})$ = 2.54 μ_B and $\mu_{eff}(Pr^{3+})$ = 3.58 μ_B, respectively. (For interpretation of the references to color in this figure legend, the reader is referred to the Web version of this article.)

strongly suggest the coexistence between trivalent and tetravalent states of Pr ions. The X-ray photoemission spectroscopy analysis of the solid-state parent sample [17] revealed that a prominent peak of Pr^{3+} is visible accompanied by a smaller shoulder structure of Pr^{4+}, which is consistent with the mixed valence state of the Pr ion.

The magnetic data suggest that about half of Pr ions are oxidized to the tetravalent state over the whole range of Sb substitution. Accordingly, for the end members with x = 0 and 1.0, we assume that $Ba_2^{2+}Pr^{4+}M_{0.5}^{3+}M_{0.5}^{5+}O_6$ (M = Bi or Sb) is probably realized under the charge neutrality in contrast to $Ba_2^{2+}Pr^{3+}M^{5+}O_6$. First of all, we consider B site disordering of the parent sample on the basis of the B-site ionic radius difference $\triangle r_B$ as mentioned in the part of Introduction. For the $Ba_2^{2+}Pr^{4+}Bi_{0.5}^{3+}Bi_{0.5}^{5+}O_6$ composition, $\triangle r_B$ was decreased from 0.23 Å at the trivalent state of Pr ion to 0.045 Å at the tetravalent state, where $r_{B'}$ (Pr^{4+}) = 0.85 Å and $r_{B''}$ ($Bi_{0.5}^{3+}Bi_{0.5}^{5+}$) = 0.895 Å[9]. In addition to the smaller ion radius difference, the difference in the B' and B'' cation oxidation states $\triangle Z_B$ becomes zero in the case of Pr^{4+}. For Pr^{3+} and Bi^{5+}, $\triangle Z_B$ = 2. Considering the electrostatic repulsion between B site cations, when $\triangle Z_B$ is large, the ordered arrangement of B site cations gives lowered energy compared to the disordered ones [1]. From the view point of these two factors, we expect that the Pr^{4+} based phase favors the B-site disordering, which is consistent with the small (101) peak in the X-ray diffraction data in Fig. 1(a). In the parent compound, the mixed valence state of Pr ions is closely related to the partial disordering of B-site.

Next, we discuss the tolerance factors of the two end member samples because they are associated with the crystal structures through the ionic radii of Pr, Bi and Sb. The tolerance factor of double perovskite compounds Ba_2PrMO_6 is given by the following equation,

$$t = \frac{r_{Ba} + r_O}{\sqrt{2}\left(\frac{r_{Pr}+r_M}{2} + r_O\right)}$$

where r_{Ba}, r_O, r_{Pr}, and r_M are the ionic radii of the respective ions. For (Pr^{3+}, M^{5+} = Bi^{5+}) and (Pr^{4+}, M^{4+} = $Bi_{0.5}^{3+}Bi_{0.5}^{5+}$), we obtain t = 0.9356 and 0.9366, respectively. These values remain below the threshold value t_{mono} =∼ 0.96 for the phase boundary between monoclinic and rhombohedral structures in the phase diagram of double perovskite compounds Ba_2PrMO_6[21]. On the other hand, for (Pr^{3+}, M^{5+} = Sb^{5+}) and (Pr^{4+}, M^{4+} = $Sb_{0.5}^{3+}Sb_{0.5}^{5+}$), we have t = 0.9697 and 0.9831, respectively. It is true that the former value is below the threshold value t_{rhom} = ∼ 0.974 for the phase boundary between rhombohedral and cubic structures, but the latter increases above this critical value. This estimation strongly supports the stability of cubic structure in the Pr^{4+} dominant Ba_2PrSbO_6 compound. Our magnetic data for the end member Ba_2PrSbO_6 showed that Pr^{4+} ions occupy the majority of 60% accompanied by the minority (40%) of Pr^{3+}. Furthermore, the x-ray data for this compound also revealed the presence of the cubic crystal structure. Our experimental data support the close relationship between the valence state of Pr^{4+} and the occurrence of cubic phase through the tolerance factor. For the intermediate composition $Ba_2PrBi_{0.5}Sb_{0.5}O_6$, we identified the monoclinic and cubic phases with Ba_2PrBiO_6 and Ba_2PrSbO_6, respectively. The coexistence of these two phases is also explained on the basis of the above scenario concerning the two end member compositions.

We demonstrate the optical properties for the $Ba_2Pr(Bi_{1-x},Sb_x)O_6$ (x = 0, 0.1, 0.5, and 1.0) powder samples measured by the diffuse reflectance method. First, the observed reflectance data for the powder samples are transformed to the absorption coefficient α_{KM} by using the conventional Kubelka-Munk function. Next, for the Kubelka-Munk conversion data near the band edge, we extrapolate the tangent line to the ε_p axis and evaluate the optical band gaps from the intersection according to the equation of

$$(\alpha\varepsilon_p)^n \propto (\varepsilon_p - E_g),$$

where α, ε_p, and E_g are the absorption coefficient, the photon energy, and the band gap energy [6,7]. Here, it should be noted that the power exponent n on the left hand side of the above formula decides the types of photon transition of optical absorption. For direct and indirect semiconductors, we assume that n = 2 and n = 1/2, respectively [6,7]. The optical measurements determine whether the energy gap is direct or indirect. Fig. 4 shows the absorption coefficient as a function of photon energy. For the x = 0 and 0.1 samples, we adopt $(\alpha_{KM}\varepsilon_p)^{1/2}$ vs ε_p plot.

In Fig. 4 (*b*), the square of the absorption coefficient for the x = 0.5 and 1.0 samples, $(\alpha_{KM}\varepsilon_p)^2$, is plotted as a function of ε_p. We estimate E_g = 1.06 eV at x = 0 and 2.71 eV at x = 1.0, assuming indirect and direct photon transitions, respectively. The magnitude of the energy band gap is substantially enhanced with increasing Sb content. When the Sb content exceeds 50 %, the nature of photon absorption is changed from the indirect to direct transitions. We give some comments on the optical property for the Sb50% substituted sample. As discussed above, the crystal structure of the present sample is explained by a two-phase mixture of monoclinic and cubic structures. The corresponding optical data are fitted using both indirect and direct transition models in the photon energy region between 1 and 2 eV. The former energy gap is estimated to be ∼1.12 eV, which is similar to the values of the monoclinic single phase x = 0 and 0.1 samples. However, the latter (1.43 eV) is quite different from 2.71 eV at the cubic single phase x = 1.0 sample. This reason has not been made clear but it has some relationship with chemical interaction between the two-phases such as partial substitution of the Bi ions at Sb sites of the cubic phase.

Next, we conducted the gaseous IPA degradation experiment under a visible light irradiation, to evaluate photocatalytic activities of the powder samples. Fig. 5 (*a*) shows the concentration of evolved CO_2 as a function of visible light irradiation time for the Sb-substituted Ba_2PrBiO_6. For comparison, the data for the solid state samples are presented. Here, we note that the concentration is normalized by the surface area of the powder samples listed in Table 1. The CO_2 concentrations for both the parent and x = 0.1 citrate samples show a rapid rise at the initial 20 min under the visible light irradiation and then increase gradually with increasing irradiation time. The stable photocatalytic efficiency after 20 min is related to the absorption process of photogenerated CO_2 on the surface of samples, which contributes to reduction of CO_2 concentration.

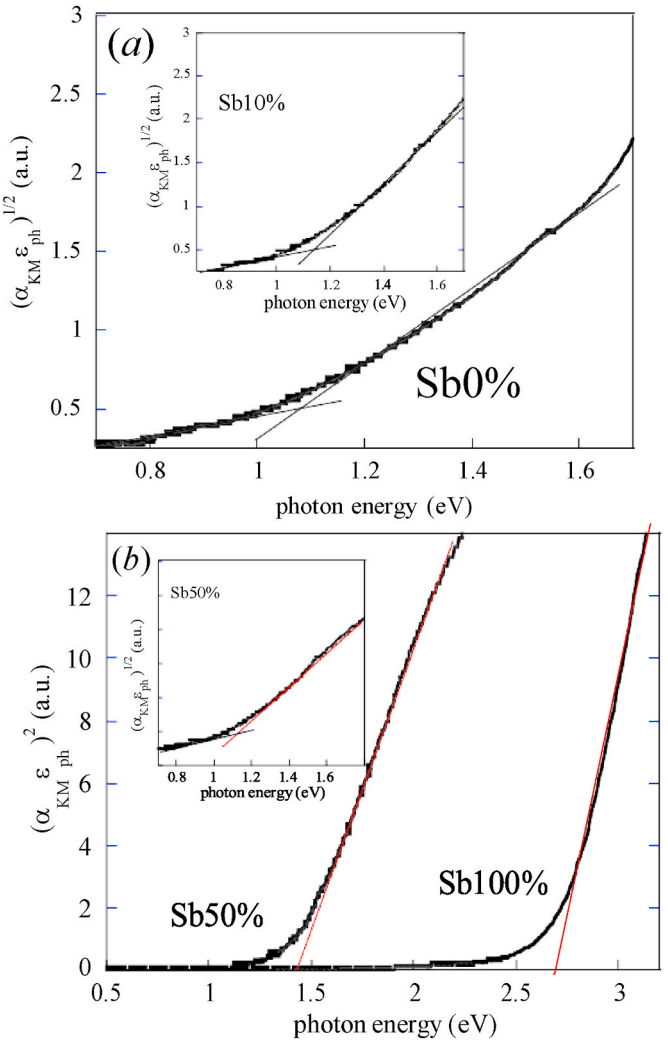

Fig. 4. (color online) Optical properties of $Ba_2Pr(Bi_{1-x},Sb_x)\ O_6(x = 0, 0.1, 0.5,$ and 1.0). (*a*) Plots of $(\alpha_{KM}\varepsilon_p)^{1/2}$ vs ε_p. For the $x = 0$ and 0.1 samples, *Eg* is estimated from an intersection point of base line and straight line by extrapolation. In the inset, the $x = 0.1$ data are shown. (*b*) $(\alpha_{KM}\varepsilon_p)^2$vs ε_p for the $x = 0.5$ and $x = 1.0$ samples are plotted as a function of ε_p. The inset denotes plots of $(\alpha_{KM}\varepsilon_p)^{1/2}$ vs ε_p for $x = 0.5$. The corresponding optical data are fitted using both indirect and direct transition models in the photon energy region between 1 and 2 eV. The former and latter band gap energies are estimated to be ~1.12 eV and 1.43 eV, respectively. (For interpretation of the references to color in this figure legend, the reader is referred to the Web version of this article.)

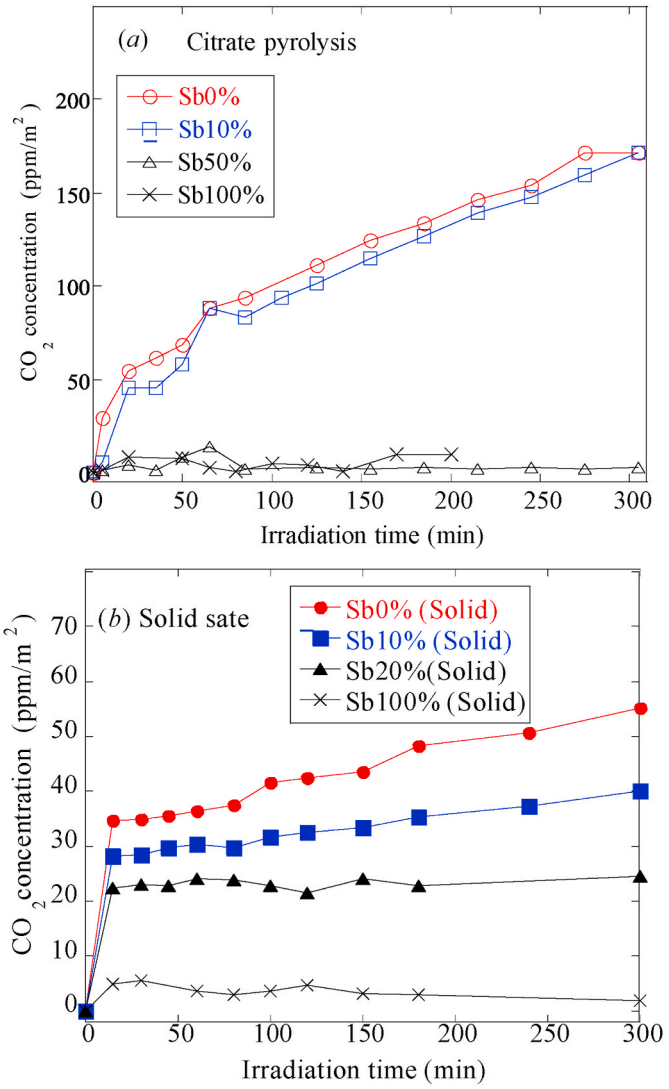

Fig. 5. (color online)Photocatalytic activities vs visible light irradiation time for Sb-substituted Ba_2PrBiO_6. (*a*) citrate pyrolysis samples, and (*b*) solid-state samples. The gaseous concentration is normalized by the surface area of the powder samples listed in Table 1. (For interpretation of the references to color in this figure legend, the reader is referred to the Web version of this article.)

On the other hand, for the Sb50% and Sb100% substituted samples we detect no clear evolution. We suspect that the band gap opening due to the heavy Sb substitution suppresses the formation of electron-hole pairs, causing a decrease of the photocatalytic reaction processes. In our previous study [22], the effect of the band gap opening due to the atomic substitution was examined by using first-principles electric structure calculation. The Sb substitution at Bi site gives rise to a reduction of the Bi-orbitals and then results in the enlarged band gap. The collapse of photocatalytic activity is probably originated from the larger band gap, which is closely related to the removal of Bi orbitals in the electric structures. The photocatalytic performance strongly depends on the Sb substitution, accompanied by an increase of the band gap energies. The photocatalytic data for the solid state samples with the same composition also show similar behaviors as the citrate samples. However, the evolved CO_2 values of the $x = 0$ and $x = 0.1$ citrate samples are more than twice as large as the data of the corresponding solid state samples, as shown in Fig. 5 (*b*). The enhanced photocatalytic properties in the citrate samples are attributed to their morphology, where fine particles are homogeneously distributed with a sub micron order. From the data listed in Table 1, we conclude that the parent and low Sb substituted samples exhibit good catalytic performance among the same synthesis based material members.

Finally, we discuss the charge separation model for higher activities of the parent Ba_2PrBiO_6 compound, as shown in Fig. 6. As far as we know, there are two approaches such as modification of the band gaps and improvement of the photogenerated charge separation in the photocatalystic materials, for completing high performance [13–15,23]. We carried out the former approach by larger Sb substitution at Bi site in the double perovskite parent compounds as mentioned before. Here, we focus on the valence mixing states between Pr^{3+} and Pr^{4+} from the view point of charge separation. As shown in Fig. 6, it is assumed that the band gap at the cluster region occupied by the $Pr^{4+}O_6$ octahedra is narrower than that at its neighboring region occupied by the $Pr^{3+}O_6$ octahedra. For the Pr^{4+} ions, the valence of their surrounding Bi ions is expected to change from 5+ to 3+ under electric neutral condition. Accordingly, the band gap becomes narrower in the presence of the $Pr^{4+}O_6$ octahedra because 6s electrons are added to empty orbitals of

Table 1
Physical and photocatalytic properties for $Ba_2Pr(Bi_{1-x},Sb_x)O_6$ compounds (x = 0, 0.1, 0.2, 0.5 and 1.0). Synthetic method, crystal symmetry, effective magnetic moment, energy gap, surface area, and gas evolution of CO_2 are listed as a function of Sb content. The value of evolved CO_2 is evaluated after a visible light irradiation of 120 min. In details, see the text (* see the caption of Fig. 4(b)).

Sb content x	Synthetic method	Crystal symmetry	μ_{eff} (μ_B)	E_g (eV)	BET (m^2/g)	CO_2 (ppm/m^2)
0.0	citrate pyrolysis	monoclinic	3.08	1.06	1.31	111
0.1	citrate pyrolysis	monoclinic	3.05	1.13	2.88	102
0.5	citrate pyrolysis	mon./cubic	3.07	1.43/1.12*	2.72	<5
1.0	citrate pyrolysis	cubic	3.0	2.71	–	<5
0.0	solid-state reaction	monoclinic	3.15[a]	1.1[a]	1.23	42
0.1	solid-state reaction	monoclinic	3.15[a]	1.17[a]	1.58	33
0.2	solid-state reaction	monoclinic	3.12[a]	1.24[a]	1.49	22
1.0	solid-state reaction	rohmbohedral	–	2.22[a]	–	~5

[a] See ref. [22].

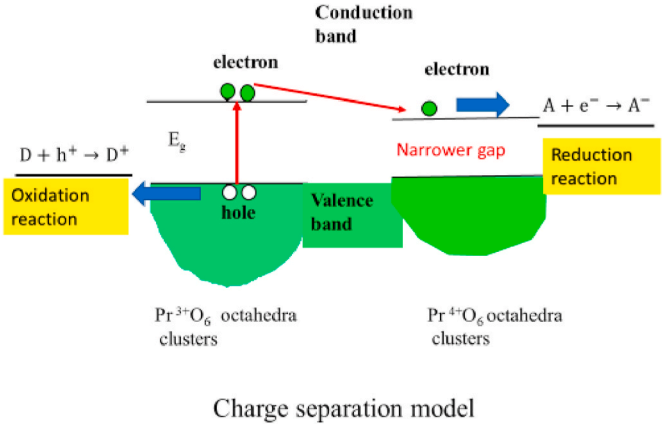

Fig. 6. (color online) Charge separation model for the coexistence between trivalent and tetravalent states of Pr ions. The band gap at the cluster region occupied by the $Pr^{4+}O_6$ octahedra is assumed to be narrower than that at its neighboring region occupied by the $Pr^{3+}O_6$ octahedra. (see the text). (For interpretation of the references to color in this figure legend, the reader is referred to the Web version of this article.)

Bi^{5+} contributing to a majority of valence and conduction bands [18]. The ptotoexcited electrons from the lower valence to upper conduction band do not recombine with holes, but transfer to its neighboring lower conduction band, resulting in charge separation. It has been reported that the Pr based compound with different valence states exhibits the highest efficiency among Ba_2ReBiO_6 series (Re = rare earth ions such as La, Pr, Ce, Nd, Sm, Eu, Gd, and Dy [6]. In previous studies on the crystal structure and magnetic properties of Ba_2ReBiO_6, the Pr ion only is shown to exist in trivalent and tetravalent states (except for Ce) [21]. Therefore, we believe that our proposed model qualitatively describes one of the possible reasons for the efficient performance of the parent Ba_2PrBiO_6 compound.

4. Summary

We investigated the crystal structures, magnetic, and photocatalytic properties of the B-site substituted double perovskite $Ba_2Pr(Bi_{1-x}Sb_x)O_6$ (x = 0, 0.1, 0.2, 0.5 and 1.0) synthesized by the citrate pyrolysis precursor method. For comparison, the photocatalytic data for the solid-state sample were examined. The present synthesis procedure enabled to prepare highly homogeneous and fine powders. The single-phase poly crystalline samples with the light Sb substitution crystallized in a monoclinic structure ($I2/m$). Magnetization measurements showed that the effective magnetic moments are located around 3 μ_B , indicating the valence mixing states between Pr^{3+} and Pr^{4+}.

The magnitudes of band gap energy for the two end member samples were estimated from the optical measurements to be E_g = 1.06 eV at x = 0 and 2.71 eV at x = 1.0. The magnitude of the energy band gap is substantially enhanced with increasing Sb content. When the Sb content exceeds 50 %, the nature of photon absorption is changed from the indirect to direct transitions. The photocatalytic performance strongly depends on the Sb substitution accompanied by an increase of the band gap energies. The photocatalytic activities of the citrate powder samples with the light Sb substitution are considerably enhanced in comparison with those values of the samples prepared by the conventional solid state method. We believe that our charge separation model qualitatively describes one of the possible reasons for the efficient performance of the parent Ba_2PrBiO_6 compound in the presence of trivalent and tetravalent states of the Pr ions. The mixed valence state of Pr ions is not only related to B site partial disordering in the monoclinic phase, but also has close relationship with occurrence of the cubic phase in the phase diagram of the double perovskite compounds Ba_2PrSbO_6.

We tried the two approaches to controlling the band gaps and realizing the photogenerated charge separation in the photocatalystic materials through larger Sb substitution and the valence mixing of the Pr ions. Our findings suggest that the higher photocatalytic activities strongly depend on the powder preparation method as well as the modification of band gaps and the photo-induced charge separation.

Declaration of competing interest

The authors declare that they have no known competing financial interests or personal relationships that could have appeared to influence the work reported in this paper.

Acknowledgement

This work was supported in part by MEXT Grands-in-Aid for Scientific Research (JPSJ KAKENHI Grants No. JP19K04995), Iketani Science and Technology Foundation, and The Mazda Foundation. We thank Mr. K. Sasaki and M. Ito for the SEM measurement.

Appendix A. Supplementary data

Supplementary data to this article can be found online at https://doi.org/10.1016/j.solidstatesciences.2020.106352.

References

[1] S. Vasala, M. Karppinen, Prog. Solid State Chem. 43 (2015) 1–31.
[2] K.-I. Kobayashi, T. Kimura, H. Sawada, K. Terakura, Y. Tokura, Nature 395 (1998) 677.
[3] R. Ramesh, N.A. Spaldin, Nat. Mater. 2 (2007) 21.
[4] A. Fujishima, K. Honda, Nature 238 (1972) 37.

[5] H.W. Eng, P.W. Barnes, B.M. Auerand, P.M. Woodward, J. Solid State Chem. 175 (2003) 94.
[6] T. Hatakeyama, S. Takeda, F. Ishikawa, A. Ohmura, A. Nakayama, Y. Yamada, A. Matsushita, J. Yea, J. Ceram. Soc. Jpn. 118 (2010) 91–95.
[7] A. Matsushita, T. Nakane, T. Naka, H. Isago, Y. Yamada, Yuh Yamada, Jpn. J. Appl. Phys. 51 (2012), 121802-1-5.
[8] T. William, A. Harrison, K.P. Reis, A.J. Jacobson, L.F. Schneemeyer, J.V. Waszczak, Chem. Mater. 7 (1995) 2161–2167.
[9] R. Shannon, Acta Crystallogr. A32 (1976) 751.
[10] L.A. Chick, L.R. Pederson, G.D. Maupin, J.L. Bates, L./E. Thomas, G.J. Exarhos, Mater. Lett. 10 (1990) 6–12.
[11] K. Koyama, A. Junod, T. Graf, G. Triscone, J. Muller, Physica C 185–189 (1991) 66–70.
[12] M. Hagiwara, T. Shima, T. Sugano, K. Koyama, M. Matsuura, Physica C 445–448 (2006) 111–114.
[13] X. Chen, S. Shen, L. Guo, S. Mao, Chem. Rev. 110 (2010) 6503–6570.
[14] D. Sudha, P. Sivakumar, Chem. Eng. Process 97 (2015) 112â€–133.
[15] B. Ohtani, Catalysts 3 (2013) 942–953.
[16] Kawachi, N. Sato, E. Suzuki, S. Ogawa, K. Noto, and M. Yoshizawa, Physica C, vol. 357–360, 1023-1026.
[17] K. Onodera, T. Kogawa, M. Matsukawa, H. Taniguchi, K. Nishidate, A. Matsushita, M. Shimoda, J. Phys. Conf. Ser. 969 (2018), 012122-1-6.
[18] J.W. Tang, Z.G. Zou, J.H. Ye, J. Phys. Chem. C 111 (2007) 12779–12785.
[19] T. Murase, H. Irie, K. Hashimoto, J. Phys. Chem. B 108 (2004) 15803–15807.
[20] W.T. Fu, D.J.W. IJdo, J. Solid State Chem. 178 (2005) 2363–2367.
[21] S. Otsuka, Y. Hinatsu, J. Solid State Chem. 227 (2015) 132–141.
[22] H. Taniguchi, M. Matsukawa, K. Onodera, K. Nishidate, A. Matsushita, IEEE Trans. Magn. 55 (2) (2019).
[23] C. Karthikeyan, Prabhakarn Arunachalam, K. Ramachandran, Abdullah M. Al-Mayouf, S. Karuppuchamy, J. Alloys Compd. 828 (2020) 154281.